ACOUSTIC CHARGE TRANSPORT DEVICES

This article describes the principles of device operation, simple models, design issues, and applications of acoustic charge transport (ACT), surface acoustic wave (SAW), and electroluminescent display devices. Emphasis is placed on conveying a clear understanding of the physical concepts so that a new investigator may gauge the capabilities of the device, while a practicing device engineer can learn about theoretical background, design principles, and application issues. Applications of acoustic charge transport devices include high-speed pattern recognition, real-time image processing, radar target emulation, frequency agile serial modulation, adaptive receiver processing, and programmable intermediate frequency (IF) filters and channelizers. Electroluminescent devices have applications in the rapidly emerging technologies of flat panel displays and head-mounted displays. The article is divided into two parts. The first part describes the SAW and ACT devices and the second part deals with electroluminescent display devices.

Many applications, such as radar target identification and high-speed pattern recognition, call for a real-time correlation of incoming electrical signals against a stored library of reference functions. Signal processing algorithms for accomplishing this correlation task involve time delays, multiplications, and additions. Acoustic charge transport devices have been used for such applications because an ACT is basically a delay line in which the input signal consists of a series of discrete charge packets. These charge packets travel in a depleted transport channel induced in a gallium arsenide substrate. Different time delays can be obtained by sensing the charge packets at different points as they travel down the delay line.

Hunsinger and Hoskins demonstrated the first ACT device in 1982 (1). Since then, ACT has been used in signal processors that can handle high-speed analog radio frequency (RF) and microwave signals. These processors have been shown to perform as many as 45 billion multiply-and-accumulate (MAC) operations per second (1–5). Charge packets in ACT devices are generated and transported by electric fields produced by piezoelectric coupling to a propagating SAW. Even though the ACT device uses surface acoustic waves, it is significantly different from the traditional SAW device. In a SAW device the signal information is contained in the surface acoustic wave itself. In an ACT device, all signal information is contained in the charge packets rather than in the SAW; SAW is used only as a parametric pump or clock. Many undesirable second-order effects of SAW devices, like parasitic acoustic reflections, are not present in ACT because charge packets are not affected by them.

To understand the operation of an ACT device, one needs to know the operation of SAW devices. Accordingly we begin with the SAW. Surface acoustic wave devices are based on the propagation of acoustic waves in piezoelectric materials. In piezoelectric crystals, application of mechanical stress produces electric polarization; this is the direct piezoelectric effect. In the converse effect, the crystal becomes strained when an electric field is applied. Piezoelectric materials like quartz and barium titanate contain a large number of electrical dipoles, which can be aligned to yield high polarization and a very high dielectric constant. The piezoelectric effect is exploited in SAW devices. The high dielectric constant characteristic makes them suitable for use in electroluminescent display devices.

SURFACE ACOUSTIC WAVE DEVICES

These devices are based on the propagation of acoustic waves in elastic solids and the coupling of these waves to electrical charge signals via electrodes deposited on the piezoelectric material. Propagation of acoustic waves on the surface of elastic solids was described by Lord Raleigh in 1885. However, it was the invention of the interdigital transducer (IDT) by White and Voltaire in 1965 that provided a practical method for generating and detecting these acoustic waves. This spurred a worldwide research effort in SAW devices; they are called surface acoustic wave devices because the velocity of the waves traveling on a piezoelectric material surface is approximately 3000 m/s, which is in the acoustic velocity range. Several SAW devices, such as the linear phase filter, oscillator, correlator, and pulse compressor, were developed during the 1970s and found applications in digital signal processing (DSP), radar system components, and frequency domain filters. Now, they also play a key role in consumer and communication systems because of their high performance, small size, low cost and high reproducibility (6–9). Every television set produced today contains at least one SAW filter. It is used in the IF stage of the receiver, where it selects the channel and forms the spectrum. Also, SAW filters can be used for separating the video signal from the sound signal. For multistandard television sets, there are available switchable filters that change their amplitude and group delay characteristics when a single external switch is closed. This means that a single filter suffices to receive television signals of different standards. Satellite receivers contain SAW filters at center frequencies varying from 400 to 500 MHz. Also, SAW resonators have traditionally found widespread application in oscillator circuits. This application has become important because of the trend toward higher frequencies in remote control systems.

Principle of Device Operation

A large number of SAW devices are essentially tapped delay lines with a potentially very high tap density and with the amplitude and phase at each tap capable of precise control. The devices usually are operated at frequencies between 30

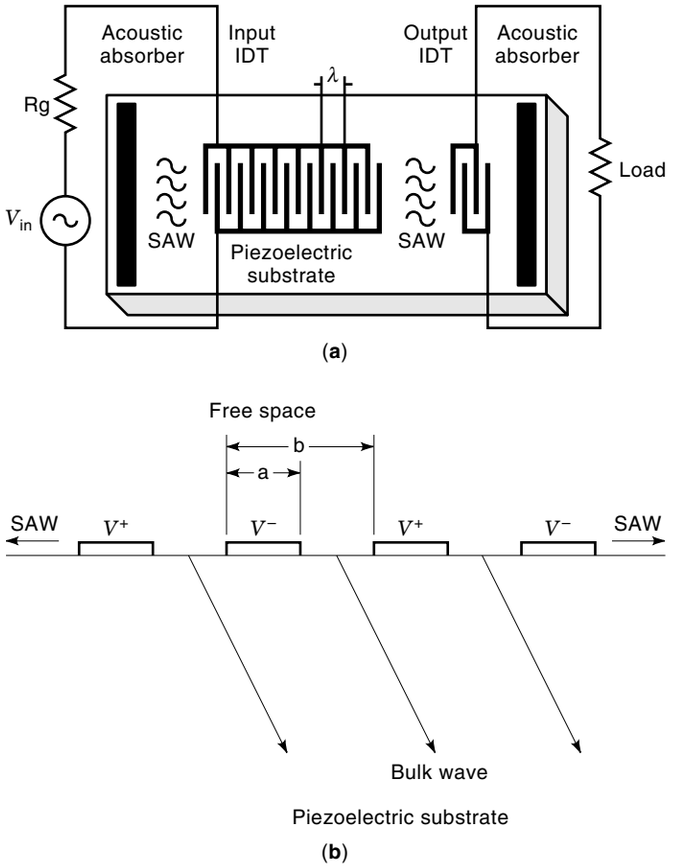

Figure 1. Basic configuration of a SAW device with input and output interdigital transducer, (a) top view, (b) side view. Electrical excitation at the input IDT injects an acoustic wave into the material. This wave is detected by the output IDT after a controllable delay.

and 300 MHz, although higher and lower frequencies have been used. Surface wave devices can have high fractional bandwidths, in theory about an octave. Nondispersive delay lines are the simplest devices conceptually, yet they have great use throughout electronic systems. Their description will serve to introduce the fundamentals of surface wave structures.

The basic configuration of a SAW device is shown in Fig. 1. Its delay line is made up of two interdigital transducer arrays separated by a distance L, with time delay $t = L/v$, on a piezoelectric substrate. An ac voltage applied to the input comb structure causes a distortion in the material between the fingers due to the piezoelectric effect. This periodic strain produces an acoustic wave that propagates away from the input transducer in both directions with a frequency equal to that of the applied signal. In one direction, the acoustic wave is absorbed in a lossy medium. In the other direction, the wave propagates to the output transducer and is detected by the inverse piezoelectric effect. These surface waves are called Rayleigh waves. In a solid the simplest type of elastic wave is a longitudinal wave in which the material is alternately compressed and expanded. A second type of elastic wave, the transverse wave, is involved with the shear of the material when the wave passes through it. For an isotropic material with free surface and a finite cross section, the combination of shear and longitudinal waves results in the Rayleigh wave. An important characteristic of a surface wave is that most of its energy is confined to a depth of approximately one wavelength.

Interdigital transducers are used to exploit the surface wave propagation for signal processing applications. A piezoelectric material has the characteristic of being elastic and generating an electric field when a force is applied to it and vice versa. Wave propagation on the surface of the piezoelectric material can thus be launched and detected by metal electrodes deposited on the surface of the material [Fig. 1(a)].

When a voltage is applied to the input IDT, electric fields are created on the electrodes that excite alternating stress patterns via the piezoelectric effect. The electric field is reversed at each electrode, and therefore, at frequencies for which the periodic length l of the array is an odd number of wavelengths, elastic surface waves are launched in both directions normal to the electrodes due to constructive interference. If v is the surface wave velocity for the piezoelectric material, the frequencies of elastic resonance are $(2n - 1)v/l$, where n is an integer. The fundamental resonance frequency (f_0) occurs when $n = 1$. Since the piezoelectric effect is reversible, the output IDT on the other end will pick up the electric field associated with the forward traveling wave and transfer it to the load. To summarize, the signal to be processed is converted into mechanical vibrations through the input IDT, propagates as a SAW with an elastic wave velocity that is material dependent, and is finally detected by the output IDT where the mechanical energy is converted back to electric energy.

The discussion above assumes uniform finger overlap or unapodized fingers. However, the fingers can have nonuniform overlap (apodized fingers). Apodization can change the impulse response of the IDT, because the geometric finger pattern corresponds to a spatially sampled replica of the IDT impulse response, and the amount of energy radiated is proportional to the amount of finger overlap. Consider the impulse response of a bandpass filter as an example. If the frequency response of the filter is ideal, the corresponding impulse response is a sine function. Thus the geometric pattern of the finger overlap should be in the form of a sine function. Apodizing fingers can also be considered as a weighting function to the impulse response.

Actually, the electric field excites additional modes of often undesirable waves, which propagate inside the substrate. The generation of these waves is determined by the piezoelectric constant of the substrate, which in turn is determined by the cut of the piezoelectric material. Therefore, it is necessary to find the optimum cut of the material to avoid the generation of these waves. Figure 1(b) illustrates bulk waves that are generated and propagate at an angle with respect to the normal to the surface. These bulk waves will be reflected at the bottom of the substrate and travel to the output IDT causing interference. This and other second-order effects (10) are listed in Table 1 and are discussed next.

Second-Order Effects

Electromagnetic feedthrough or crosstalk is the direct coupling of signals from the input IDT to the output IDT in the form of electromagnetic radiation. Since the feedthrough oc-

Table 1. Piezoelectric Material Characteristics

Material	Orientation	Velocity (m/s)	k_2 (%)	Temperature Coefficient in ppm°C	N_{opt}
$LiNbO_3$	Y,z	3488	4.5	94	4
$LiNbO_3$	1280	3992	5.3	75	3.5
$LiTaO_3$	Y,z	3230	0.72	35	10.5
GaAs	(I10)	<2841	<0.06	−49	
Quartz	St,X	3158	0.11	0	22

curs at the speed of light, it interacts with the SAW signal arriving at the output IDT. The interaction results in periodic ripples of amplitude and phase across the SAW filter passband (11).

Multiple-transit interference is the result of multiple reflections and regeneration of acoustic waves between bidirectional input and output IDTs. Surface acoustic wave power arriving at the output IDT will be partially reradiated back to the input IDT due to the regenerative effects caused by current flow in the output IDT, which will cause further regeneration of acoustic waves. Ultimately the output will be corrupted by these multiple reflected waves.

Electrode finger reflections are the reflections of SAW at the edges of electrodes. These reflections are caused by mass-loading discontinuities. The mass and electrical shorting effects of the electrode change the velocity of propagation and characteristic surface wave impedance of the region around the electrode. This change will result in reflections of the surface wave from the front and back of each electrode. To reduce this undesirable effect, the mass of the electrodes is made as small as possible. Sometimes, split-electrode geometry is also used (11).

Bulk wave interference, as mentioned before, can cause additional voltage at the output IDT; distortion of amplitude, phase, and group delay; change in input impedance level; and an increase in insertion loss. Roughing the bottom surface of the substrate and coating it with a soft conductor such as silver epoxy is one way to reduce reflection of bulk waves.

Circuit factor loading is the result of finite source and load impedance. The input and output impedance of the SAW device is frequency dependent and as a result the voltage division between the device and the load becomes frequency dependent.

Diffraction occurs in SAW IDTs just like it occurs in optical systems. Ideally all parts of the wavefront of the wave should arrive at the receiving IDT with the same delay. However, the SAW wavefront is spherical, to the degree that it is dependent on the aperture of the radiating source, and this will corrupt the response. One method to overcome diffraction is the use of unequal length split-electrodes and dummy fingers (11).

Apart from diffraction, the receiving IDT also will be unable to intercept the entire incident SAW beam because of beam steering. These losses are the result of fabrication misalignment. Piezoelectric materials are anisotropic, and, if the receiving IDTs are misaligned with respect to the desired crystal propagation, some of the incident wave energy is lost. Beam steering losses are independent of frequency but proportional to IDT width and degree of IDT misalignment for a given substrate.

Acoustic Charge Transport Device

Figure 2 shows the schematic of an ACT device configuration (12). Generation and propagation of charge packets in gallium arsenide is due to electric fields produced by the piezoelectric coupling to the propagating SAW. These charge packets constitute the signal in the ACT device. Note that the SAW itself is generated directly on the piezoelectric gallium arsenide. Since the signal is in the charge packets and not in the wave, many undesired second-order effects of SAW, like the parasitic acoustic reflections do not occur in ACT. It is important to isolate the charge packets from the interface state traps at the junction of the substrate and the epitaxial gallium arsenide layer. This is accomplished by increasing the thickness of the epitaxial layer to an appreciable fraction of the SAW wavelength at the clock frequency. The charge packets are confined to a transport channel in the epitaxial layer and the ACT device has high transport efficiency because it operates in a buried channel mode instead of a surface mode.

Another important feature of an ACT device is nondestructive charge sensing. The charge in the packet is sensed via the image charge induced in the metal features fabricated within the propagation path.

Principle of Operation

The transport channel in the ACT device of Fig. 2 is defined by the metal/n-GaAs Schottky diode and the potential barrier between the n-GaAs and the semi-insulating GaAs substrate. Electric voltage bias is applied to the metal electrode and the substrate in such a way that the n-GaAs region is depleted of electrons (majority carriers) and a potential barrier exists between the n-GaAs and semi-insulating GaAs layers (13). The depletion of n-GaAs is accompanied by the creation of a static potential well in this layer (1). The spatial variation of depletion potential in the n-GaAs channel layer can be derived by using the depletion approximation (14) and is para-

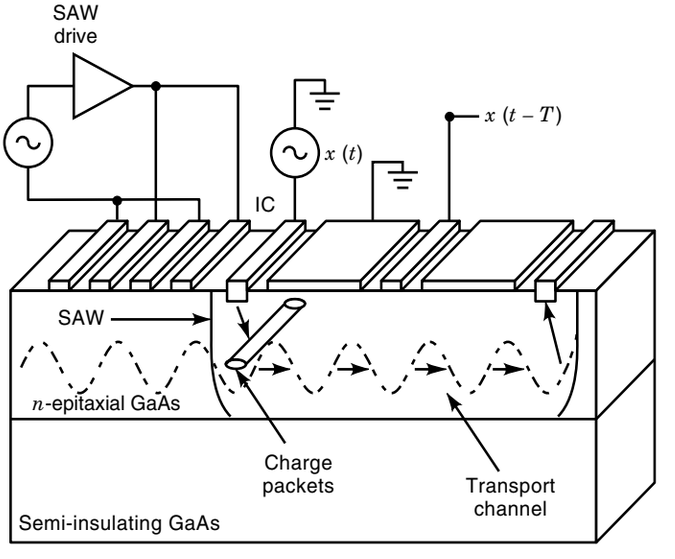

Figure 2. Acoustic charge transport device configuration. Interaction between the SAW and the static depletion potentials leads to three-dimensional potential wells which can capture and propagate charge (introduced by $x(t)$) in the transport channel.

bolic. The depletion of the n-type channel is also accompanied by the buildup of negative space charge in the semi-insulating substrate through the filling and emptying of deep traps (15). In computing the depletion potential, the semi-insulating substrate can be treated as though it had an acceptor concentration approximately equal to the unoccupied deep trap density in the bulk of the material.

Surface acoustic waves generated by an interdigital transducer propagate through the depleted channel layer, creating traveling wave potential wells that move at the velocity of sound. When the wave amplitude is sufficiently large, mobile electrons injected into the channel by $x(t)$ bunch into charge packets, which propagate in synchronism with the wave at the velocity of sound. As in a conventional charge coupled device (CCD), these charge packets can be sensed destructively via an output ohmic contact or nondestructively via capacitive coupling to electrodes on the surface of the device. Note that the metal at the surface of the device shorts the wave potential so that the SAW also serves to confine the mobile charge. From a calculation of the variation of SAW potential magnitude (16) in [100] cut GaAs for a ⟨110⟩ propagating wave, one can show that the thickness of the channel layer must be on the order of an acoustic wavelength to optimize the channel potential imposed by SAW.

Although the device structure shown in Fig. 2 can be biased with both the Schottky metal and the substrate at the same potential, it is usually desirable to apply a bias between the two, so that the electron potential minimum associated with the static depletion potential coincides in position with the SAW magnitude maximum. This is desirable because the charge capacity of the wave is maximum when the charge transport occurs in the region of maximum wave potential.

Interaction between the SAW and the static depletion potentials leads to three-dimensional potential wells, which propagate at the velocity of sound. The equipotential surfaces of these wells resemble cylinders shown in Fig. 2.

The total channel potential has four components: (1) the depletion potential, (2) the SAW potential, (3) potential due to the mobile charge in the transport channel, and (4) potential due to the induced charge on the conductors in proximity to the channel. All of these contributions must be taken into account while analyzing (1) the charge capacity of the ACT device.

For the proper operation of the ACT device, the wave electric field should be greater than the synchronous field value given by $E_s = -V_s/\mu$ where V_s is the SAW velocity and μ is the electron (carrier) velocity. Then the charge carriers are effectively trapped in the large potential wells of the SAW and are constrained to move with the wave at the velocity of sound.

On the other hand, when the wave electric field is smaller than E_s, the mobile charge injected into the channel will continually slip back in the wave, since the electric field is not large enough to transport charge at the velocity of sound. This is the small signal acoustoelectric effect (17).

Detailed theoretical analysis of the charge transfer characteristics of the buried channel ACT device implemented in high-mobility materials (where the channel center to image conductor separation is approximately one-fourth of an acoustic wavelength or greater) was performed by Hoskins and Hunsinger (1). It was found that

1. The active channel layer must be half of an acoustic wavelength or greater to optimize the capacity of the wave.
2. Diffusion-induced transfer inefficiency will not significantly limit the transport performance of the ACT device for wave potentials greater than approximately $\frac{1}{2}$ V.
3. The transport performance is relatively insensitive to electron mobility if the wave electric field is much greater than the synchronous field.
4. The equivalent sheet charge capacity of the transport process increases linearly with wave frequency.

The charge capacity, signal bandwidth, time-bandwidth product, and device compatibility with thin epitaxial layers are enhanced by increasing the operating frequency of the ACT device.

The Electromechanical Coupling Coefficient

This coefficient is a characteristic of the piezoelectric material and is a measure of the efficiency of transduction from electrical to mechanical energy. In standard tensor notation, the propagation of acoustic waves in an arbitrary anisotropic piezoelectric medium (18) is described by the following set:

$$\frac{\partial T_{ii}}{\partial x_i} = \rho \frac{\partial^2 u_i}{\partial t^2} \tag{1}$$

$$S_{kl} = \frac{1}{2}\left(\frac{\partial u_k}{\partial x_l} + \frac{\partial u_l}{\partial x_k}\right) \tag{2}$$

$$\frac{\partial D_l}{\partial x_i} = 0 \tag{3}$$

$$E_i = \frac{-\partial \varphi}{\partial x_i} \tag{4}$$

$$T_{ij} = c^E_{ijkl} Skl - e_{nij} En \tag{5}$$

$$D_m = e'_{\mathrm{mkl}} S_{kl} + s_{\mathrm{mn}} E_n \tag{6}$$

In these equations, T is the stress, ρ is the mass density, U is the mechanical displacement, S is the strain, D is the electric displacement, E is the electric field, and φ is the electric potential. The stress T represents the force F applied per unit area A, and the strain S represents the fractional deformation due to the force F. The primed quantities, that is, the elastic constants c'_{ijkl}, the piezoelectric constants e'_{ijkl}, and the dielectric constant ϵ'_{ij} refer to a rotated coordinated system through the Euler transformation matrix V_{ij} (12). The superscript in the elastic constant indicates that it is measured under a constant electric field E, whereas the superscript in the dielectric constant indicates that it is measured under constant strain S. Here the elastic constant gives the mechanical relationship between stress T and strain S and the piezoelectric constant gives the electrical relationship between electric displacement D and strain S of the piezoelectric material. Equations (1) through (6) are valid only within the crystalline substrate. For the region outside the substrate, the electric potential is governed by the Laplace equation. Solutions of these equations are assumed to be of standard complex traveling-wave form in which v_s, is the wave velocity, α is the exponential

decay constant into the crystal, and ω is the steady-state angular frequency. It can be shown (12) that the solutions for the region inside the substrate are given by

$$u_i = \sum_{l=1}^{4} B^{(l)} \beta_i^{(l)} \exp\left[-\alpha^{(l)} \frac{\omega x_3}{v_s}\right] \exp\left[j\omega\left(\frac{t - x_1}{v_s}\right)\right] \quad (7)$$

$$\varphi = \sum_{l=1}^{4} B^{(l)} \beta_4^{(l)} \exp\left[-\alpha^{(l)} \frac{\omega x_3}{v_s}\right] \exp\left[j\omega\left(\frac{t - x_1}{v_s}\right)\right] \quad (8)$$

where $i = 1,2,3$. Here x_3 is the normal distance measured from the substrate surface toward the inside of the substrate, and x_1 is the parallel distance measured on the surface of the substrate toward the direction of wave propagation. In the region outside the substrate, the potential is a solution of the Laplace equation given by

$$\varphi = \sum_{l=1}^{4} B^{(l)} \beta_4^{(l)} \operatorname{csch}(\omega h / v_s) \sinh \left[\frac{\omega}{v_s}(x_3 + h)\right] \exp\left[j\omega\left(\frac{t - x_1}{v_s}\right)\right] \quad (9)$$

where h is the distance between the surface of the substrate and an infinitesimally thin perfect electric conductor on top of it. A free surface corresponds to $h = o$, whereas a shorted surface corresponds to $h = co$. The constants B and β have to be determined by mechanical and electrical boundary conditions.

From these results, it is observed that beneath the surface of the substrate, the mechanical displacement and electric potential decay exponentially into the substrate x_3 while traveling in the x_1 direction. Just above the surface of the substrate, the potential is a traveling wave in the x_1 direction. When the distance h between the electric conductor and the substrate decreases, the propagation velocity decreases due to the change from free to shorted-electrical conditions at the surface. This change is a measure of the efficiency with which a surface wave propagating on a piezoelectric substrate interacts with electrodes placed on the surface. The electromechanical coupling coefficient K^2 is used to measure this efficiency and is defined as

$$K^2 = -2\frac{\Delta v}{v} \quad (10)$$

where Δv is the magnitude of the SAW velocity change that occurs when the surface of the piezoelectric substrate is shorted by a thin highly conducting metal film and v is the unperturbed SAW velocity. This parameter is an important factor in the choice of substrate material and propagation geometry for a particular SAW device.

Fabrication of SAW Devices

A SAW device is made of metal electrodes deposited on the top of a piezoelectric substrate. The electrode widths and periods are in the 1 μm to 10 μm range. The substrate is made of a single layer of a piezoelectric material or a combination of different layers with a piezoelectric thin film on the top. Table 1 is a list of some commonly used piezoelectric crystals (11). In this table, the orientation is the cut of the crystal to obtain minimum attenuation loss. Velocity is the speed of the acoustic wave on the substrate's surface. The temperature coefficient is a measure of the change in delay with temperature change. k_2 is the electromechanical coupling coefficient; N is the number of electrode pairs needed to achieve the optimum performance of lowest insertion loss.

It is clear that $LiNbO_3$ has the highest k_2, which implies the highest efficiency, but it also has a quite large temperature coefficient. On the other hand, quartz has a zero temperature coefficient but a very low k_2.

The electrode pattern can be formed by two methods. In the first method, a thin film of metal is deposited on the substrate and the unwanted part is removed later. In the second method, metal is deposited on the unprotected area of the substrate to form the pattern. Well-established photolithography and etching techniques similar to those used in the integrated circuit (IC) industry are employed for the electrode pattern. The last fabrication step is packaging, which takes acoustic isolation into consideration. Absorbing materials are used around the crystal to absorb the acoustic waves and eliminate reflections. Sometimes matching networks are included in the package to provide electrical matching between the transducers and the input or output circuits.

Applications

Traditional SAW devices have numerous applications in radar system components and communication system components (9,19). Because of the small size, weight, power, high processing speed, and user-programmable response of ACT devices, this technology continues to provide system designers with new tools in solving high-speed signal-processing problems. Acoustic charge transport devices have found applications in radar target emulation (12,20), high-speed pattern recognition (21), frequency agile serial modulation (22), adaptive receiver processing (23), programmable IF filters and channelizers (19), and real-time image processing (24). More applications are sure to be found as this emerging technology matures in the next few years.

DISPLAY DEVICES

A display in this context is an electronic component or subsystem used to convert electrical signals into a visual image. The computer terminal using a cathode ray tube (CRT) or flat panels is one of the most important industrial applications of electronic displays. The electronic displays are used also for presentations of graphs, symbols, alphanumeric, and video pictures. It is believed widely that because of substantial reduction in size, weight, and power, flat panel displays (FPD) will replace more and more CRT displays in the near future. There are four major technologies for FPD at present: (1) liquid crystal displays (LCD), (2) plasma displays (PD), (3) field emission displays (FED), and (4) electroluminescent (EL) displays. Electroluminescent devices are all solid state, have fast response, wide viewing angle, high resolution, wide operating temperatures, and are light weight. For these reasons, they are of great commercial as well as scientific interest. Liquid crystal, plasma, and field emission displays are discussed elsewhere in this encyclopedia; accordingly, in the rest of this article we limit our discussion to EL displays.

Electroluminescent displays, like all emissive displays, are based on the phenomenon of luminescence display, which is

the nonthermal radiation of optical (luminous) energy when an electron makes a radiative transition from a higher energy level to a lower energy level. However, energy must be initially supplied to the system so that the electron could be raised (pumped) to the higher energy level in the first place. Luminescence is further classified in terms of the physical mechanism by which this *pumping* to the higher energy level is achieved. For example, if the pump happened to be another photon incident on the material, then the luminescence would be termed photoluminescence. When the pumping is done with electrical energy, then the radiation is termed *electroluminescence.* Two types of electroluminescence are encountered in display device applications; these are (1) injection electroluminescence and (2) high field electroluminescence. A light-emitting diode (LED) is an example of injection electroluminescence. In the case of an LED, electrical energy is supplied by a forward biased p–n junction in a semiconductor whereby high energy electrons are "injected" into the conduction band of the luminescent material where they fall to a lower energy level (in the valence band). This radiative transition results in the emission of photons (luminous energy); the phenomenon is called *injection electroluminescence.*

In the case of *high-field electroluminescence,* the electrical energy is supplied by a high field (of the order of 10^8 V/m), which accelerates electrons in a host material to very high velocities. Next, these high-speed electron impacts excite light-emitting centers (called activators) imbedded in the phosphor layer. Impact excitation consists of raising the energy level of an electron within the activator to a higher energy level; subsequent relaxation of this excited electron within the relaxation activator to the lower energy level results in the emission of photon (luminous energy). A major advantage of high-field electroluminescence devices over injection electroluminescence devices is that the former consume far less power and are therefore suitable for display applications where power dissipation must be kept at a minimum. Details on LED devices can be found elsewhere in this encyclopedia. In the following, we limit our attention to high-field EL devices.

High-field EL devices are generally classified as (1) ac thin film EL (ACTFEL), (2) ac power EL, (3) dc thin film EL, or (4) dc power EL. Of these four types, the first two are now commercially available. The ac power EL devices have found applications in backlighting for liquid crystal displays. But it is the ACTFEL device that is used for display pixels in flat panel laptop computers, word processors, head-mounted display applications, and so on. In the rest of this article, we confine our discussion to the ACTFEL device operation and performance issues.

A Brief History and Status of AC Thin Film Electroluminescent Devices

The first ACTFEL devices were introduced by Russ and Kennedy (25) in 1967. In 1974, an ACTFEL device with a luminance of 1000 fL (3400 cd/m^2) at 5 kHz driving frequency and a lifetime of more than 10,000 hr was announced by Inoguchi et al. (26). This device employed orange-emitting ZnS phosphor film with Mn activators. Also, Mito (27) showed that the ACTFEL devices could be used for a TV imaging system. Nine inch diagonal EL display panels became available in the 1980s and applications were found in industrial instrumentation and computers. Yellow emitting ZnS:Mn thin film EL displays are now readily available in various dimensions up to full sizes for workstations. For the 9 in. diagonal size, the power consumption is typically 10 W to 15 W and the average luminance is approximately 100 cd/m^2. Higher resolution A4-sized display devices with 1024 $\times$ 800 dots are being developed. The most common displays are the 640 $\times$ 400 and 640 $\times$ 480 pixel (9-in.-diagonal) half-page displays for personal computers and word processors. Thin-film EL displays are also found in applications where good contrast must be maintained in a very high ambient illumination environment such as in industrial instrumentation. The strongest selling point of thin-film EL display is high legibility because light is emitted from a submicrometer thick device with crisp pixel edges. Other well-known features are high contrast (>7 : 1 at 500 lux ambient with filter), wide viewing angle (>160°), fast response time (several microseconds), and the capability for very high resolution. Thin-film EL displays are addressed at video frame rate, and thus there is no smear in mouse and cursor applications. All this is achieved in a simple, solid-state device structure that is insensitive to shocks and wide temperature variations (28).

The major challenge for the EL industry at present in the development of multicolor and full-color display panels. Extensive research efforts are being directed to this end (29–30). Different phosphor materials, device structures, and color strategies (like color-by-white, which use filters to get multicolor from a white emitting ACTFEL device) are being investigated.

Alternating Current Thin Film Electroluminescent Device Configuration

To illustrate the device structure and the basic operating principle, we use a yellow-emitting ZnS:Mn ACTFEL device as an example. A schematic of an ACTFEL device configuration is shown in Fig. 3. The glass substrate provides the mechanical support; practically, the entire weight and the thickness of the ACTFEL device are equal to the weight and thickness of the glass substrate. The bottom electrode is typically indium tin oxide (ITO). It is transparent (90% transmissivity in the visible spectrum) and conductive (typical resistivity of 5 $\times$ 10^{-6} Ωm). Usually, ITO is deposited on glass by

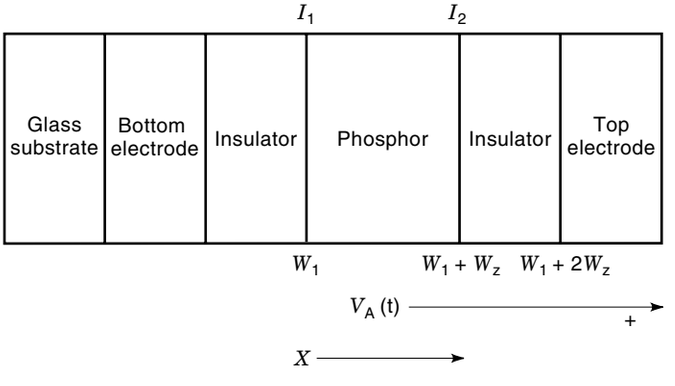

Figure 3. Schematic of an ACTFEL device. Application of high electric field between the electrodes leads to light emission from the phosphor layer.

sputtering. The top electrode can be a metal layer, because it does not have to be transparent. An example of the phosphor layer is 700 nm thick zinc sulfide film incorporating about 1% manganese activators. A commonly used method for depositing the ZnS : Mn layer is electron beam evaporation, although other methods have been used (31).

As mentioned above, electroluminescience occurs in the zinc sulfide phosphor layer when a high field (of the order of 10^8 V/m) is applied. In theory, one should be able to sandwich this phosphor layer between two electrodes, apply the suitable voltage and obtain the EL output. In practice, the thin phosphor layer tends to contain defects and impurities that can produce a localized short circuit. When that happens, a very high current is drawn resulting in a damaged device. To counter this hazard two insulating layers are added. These surround the phosphor layer (see Fig. 3). They serve as current-limiting layers because the current in the device is now limited to the capacitive charging and discharging displacement current, as long as the insulating layers themselves are not defective or *leaky*. An example of an insulating layer is a 300 nm thick aluminum oxide film deposited by RF magnetron sputtering, although many other insulating materials have been used (32). Once these two layers are added, the device can no longer be operated in a dc mode because insulating layers carry no direct current. ACTFEL is an ac, bipolar device. It is typically operated by applying a series of bipolar voltage pulses between the top electrode and the bottom electrode. Figure 4(a) shows an example of a bipolar excitation voltage waveform. Frequency is 100 Hz, voltage amplitude is 200 V, pulsewidth is 30 μs, rise time and fall time for the pulse are 10 μs each. Of the two electrodes sandwiching the insulating layers, one has to be transparent in order for the EL output to leave the device. Indium tin oxide is the typical transparent electrode. The top electrode is a conducting metal; aluminum is a typical choice because of its low melting point which adds a self-healing feature to the ACTFEL device in the following manner: in spite of the addition of the two insulating layers, practical ACTFEL devices tend to still suffer from the existence of localized pockets of very high current which cause an excessive localized heat dissipation. This heat would normally tend to spread the damage across the whole device making it useless. However, the spreading of the damage is avoided when the low melting-point aluminum electrode burns out at the local defect site of the high current path thus causing a localized open-circuit and thus limiting the damage to the local defect area. The aluminum electrode is about 75 nm thick and is deposited by thermal evaporation or sputtering.

Principle of Operation

In this section we describe the electronic processes that lead to the emission of luminous photons when the voltage of Fig. 4(a) is applied between the top electrode (aluminum) and the bottom electrode (ITO) of the ACTFEL device of Fig. 3. $V_A(t)$ is the voltage of the aluminum electrode with reference to the

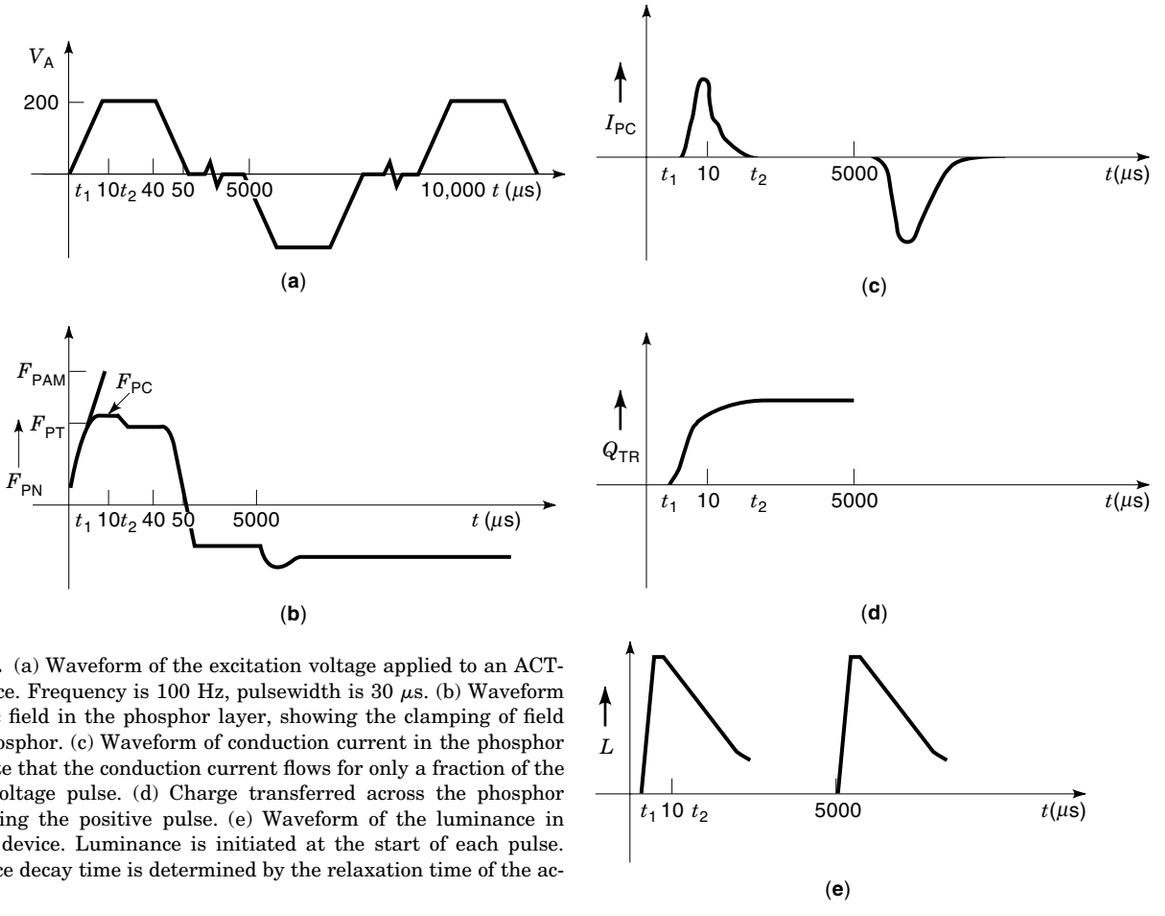

Figure 4. (a) Waveform of the excitation voltage applied to an ACTFEL device. Frequency is 100 Hz, pulsewidth is 30 μs. (b) Waveform of electric field in the phosphor layer, showing the clamping of field in the phosphor. (c) Waveform of conduction current in the phosphor layer. Note that the conduction current flows for only a fraction of the applied voltage pulse. (d) Charge transferred across the phosphor layer during the positive pulse. (e) Waveform of the luminance in ACTFEL device. Luminance is initiated at the start of each pulse. Luminance decay time is determined by the relaxation time of the activator.

ITO electrode. Thus, during the positive pulses ($0 < t < 50$ μs, for example), aluminum is the anode and ITO is the cathode; interface I_2 is the anodic interface; interface I_1 is the cathodic interface.

Below Threshold ($0 < t < t_1$). At first, the ACTFEL device appears to the voltage source as three capacitors in series; each of the insulator layers and the phosphor layer act like a capacitor and take up a fixed fraction of the applied voltage, $V_A(t)$. As $V_A(t)$ rises linearly, so does the voltage $V_P(t)$ across the phosphor layer and the electric field $F_{PA}(t)$ in the phosphor layer. $F_{PA}(t) = V_P(t)/W_z$, where W_z is the thickness of the phosphor layer. $F_P(t)$ is sketched in Fig. 4(b). Note that the direction of the field, F_P is from I_2 to I_1 (see Fig. 3). Because there are no free electrons inside the insulator and the phosphor layer, there is no conduction current even though an electric field is present. There are electrons in the valence bands of the phosphor and the insulator, but they cannot move because all the states are occupied. For a conduction current to exist in the phosphor, electrons need to be excited to the conduction band, which is at a much higher energy level than that of the valence band (by 3.6 eV; 1 eV = 1.6×10^{-19} J). Such an excitation can happen when energy is supplied to the device by an electric field, heating, or optical means. Also, there are electrons at the interfaces between the phosphor and the dielectric layers; these are trapped at midgap interface states which are only about 1 eV below the conduction band of zinc sulfide. Thus these interface electrons are easier to be excited to the conduction band than the valence band electrons.

Above Threshold ($t > t_1$). When the field $F_P(t)$ reaches a certain value, called the *threshold field* ($\sim 10^8$ V/m), say at $t = t_1$, it is able to excite electrons trapped at the interface I_1 into the conduction band of the phosphor by a process called *Fowler–Nordheim tunneling.* Now these electrons are free to move. A lot of free electrons become available and a conduction current I_{PC} begins to flow in the phosphor [see Fig. 4(c)]. It is clear that the value of the threshold field depends critically on the location of the interface state trap, which is a function of the dielectric material composition and interface conditioning (33–35). Also, the value of I_{PC} depends upon the density of the electron population at the interface I_1, which is again a function of dielectric material and interface conditioning (33–35).

Next, these free electrons accelerate in the high phosphor field and gain high velocities and energies. Let us call them *hot electrons.* Upon encountering a manganese activator (approximately 1% of atoms in the phosphor layer are manganese activators), the hot electron impact excites it. Impact excitation consists of elevating an electron inside the manganese activator from a lower energy level (E_{AL}) to a higher energy level (E_{AH} still inside manganese). In time, this excited electron relaxes back to its original lower energy state and simultaneously emits a photon of energy equal to ($E_{AH} - E_{AL}$). For manganese, this energy corresponds to a *yellow* photon. If the activator atom had been samarium (Sm), the emitted photon would have been *red* because the energy difference ($E_{AH} - E_{AL}$) in case of samarium is smaller and corresponds to the energy of a red photon. Thus, luminous photons of different energy (and color) can be caused to be emitted from this ACTFEL device by using different activator and phosphor materials.

In the meantime, the original hot electron, which had impact excited the manganese activator, continues on its way toward the other interface (I_2), called the *anodic interface.* Note that it can again impact excite more manganese atoms which it might encounter before it reaches I_2. Once the hot electron reaches the anodic interface, it encounters an insulator (insurmountably high energy barrier) and can go no further. It therefore rests at I_2 in an interface trap. A quick calculation shows that the transit time for the hot electron to reach from I_1 to I_2 is very small (less than 100 ps). On the other hand, the relaxation time for the excited electron within the manganese activator is quite large (more than 100 μs). Thus the luminescence conduction can occur long after the causative conduction current has vanished.

The luminance–time characteristic is sketched in Fig. 4(e). Note that the ACTFEL device becomes luminescent at $t = t_1$, when the conduction current is initiated. Because luminance is directly proportional to the instantaneous value of the impact excited activator atoms, it can be expected to peak at the same time as the conduction current ($t = 10$ μs). However, since the relaxation time of the manganese activators is in hundreds of microseconds, the luminance persists long after the current I_{PC} has become zero (see Fig. 4).

The luminous energy radiated at any given time is, of course, directly related to the number of manganese activators, which are impact excited, and depend on the following:

1. The number of hot electrons being transferred (conduction current). This will depend upon the available electron density at the cathodic interface and the amplitude of the applied field. If the interface states are too *deep,* then I_{PC} will be small and so will the luminance.
2. The average energy of the hot electrons. For example, if the interface states are "shallow" (close to the zinc sulfide conduction band), then conduction current will begin to flow at too low a phosphor field. This field may not be strong enough to impart sufficient energy (for impact excitation of manganese) to the hot electrons. Also, if the mean free path (before colliding with a defect or impurity) of the hot electrons is too small, then they may not be able to pick up sufficient energy from the field. Thus crystallite size and purity of the phosphor film and interface conditioning are important.
3. The concentration of manganese activators and their impact cross-sectional area. These determine the probability that a hot electron will be able to encounter an activator during its transit from interface I_1 to I_2. Excess concentration of manganese activators can result in them being so close to each other that a nonradiative transfer of energy can occur from an excited manganese activator to its nonexcited neighbor. This process continues until the energy is dissipated at a defect or impurity in the phosphor layer. This concentration quenching is detrimental to ACTFEL device luminance. High manganese concentration can also result in reduction of the mean face path for the hot electrons.
4. Uniformity of manganese activator distribution in the phosphor layer.

5. Uniformity of conduction current flow across the phosphor layer (36).
6. Light-trapping effect caused by the total internal reflection of the emitted photons in the phosphor layer. This, of course, reduces the light exiting the glass substrate.

Because of the negative charge (1.6×10^{-19} C) of a hot electron, its arrival at I_2 causes the interface to be negatively charged; also its departure from I_1 leaves that interface positively charged. These equal and opposite charges on the two interfaces produce an internal field (F_{PI}), from interface I_1 to I_2 (opposite direction from that of the applied field, which is from I_2 to I_1). Thus the effect of the transferred charge (transferred via the conduction current) is to reduce the net field (F_{PN}) in the phosphor. The net field, of course, is the difference of the applied field (F_{PA}) and the internal field (F_{PI}). $F_{PN} = F_{PA} - F_{PI}$ (see Fig. 3). The transferred charge (Q_{TR}) is simply the time integral of the conduction current, I_{PC}, and is sketched in Fig. 4(d). Let us next consider what happens to the net phosphor field (F_{PN}) after $t = t_1$: during $t_1 < t < 10$ μs, the applied voltage is increasing, which will tend to raise F_{PA} and hence F_{PN}. But during this time, I_{PC} and Q_{TR} are also increasing, which would tend to increase F_{PI} and reduce F_{PN}. The nature of the Fowler–Nordheim tunneling process is such that a very small increase in the field results in a very large increase in I_{PC} and Q_{TR}. As a result, the net field F_{PN} can be expected to register only a small increase above the threshold field F_{PT} before it clamps to a constant value called the clamping field F_{PC}. Once the phosphor field clamps, the voltage across the phosphor layer also becomes constant. All of the increase in the applied voltage V_A during the time interval between clamping and $t = 10$ μs is absorbed entirely by the two insulators. As a result, during this interval, the ACTFEL device appears like two capacitors in series (instead of three) to the voltage source. In other words, the effective device capacitance is higher than it was before clamping.

After $t = 10$ μs, the applied voltage becomes constant [Fig. 4(a)], but the conduction current is still flowing (because F_{PN} is greater than F_{PT}) and so F_{PN} decreases with time as does I_{PC}. The conduction current becomes zero as F_{PN} dips just below F_{PT} (say at $t = t_2$) and Q_{TR} stops increasing.

At $t = 40$ μs, the applied voltage begins to decrease with a corresponding linear decrease in the phosphor field F_{PA} and F_{PN}, because F_{PI} is constant (no I_{PC} change in Q_{TR}). The magnitude of total field reduction is equal to F_{PAM} at $t = 50$ μs. F_{PAM} is the value that the maximum field in the phosphor would have achieved if there were no tunnel breakdown of the phosphor layer [see Fig. 4(b)]. The negative field which exists in the phosphor between the positive and negative pulses is also called the residual field. It produces no current or luminance of its own, but makes the ACTFEL device turn on (start I_{PC}) sooner when the next opposite polarity voltage pulse arrives at $t = 5000$ μs.

When the negative voltage pulse is applied to the ACTFEL device (see Fig. 3), the old anodic interface (I_2) becomes the new cathodic interface (and vice versa). The electrons are now tunnel ejected from the interface I_2 and begin their journey back toward the interface I_1. On the way they pick up velocity and excite manganese activators in their path. Because the residual field aids the new applied field, F_{PT} is reached sooner, the conduction current I_{PC} flows longer, more charge (Q_{TR}) is transferred, and the luminance pulse is larger (see Fig. 4). The current flow is reversed in the next positive pulse, and this back and forth flow continues. After a few pulses, a steady state is reached when the charge transferred (Q_{TR}) is the same in either direction (37). In steady state, an equal number of electrons is transferred back and forth; however, if the two interfaces (I_1 and I_2) do not have identical composition, the two electron distributions will not be equal. As a result, the average energy of hot electrons leaving I_1 may be different from the average energy of electrons leaving I_2. Consequently, the efficiency of manganese excitation may be different, and hence the luminance pulses for positive and negative voltage pulses may not be identical even in the steady state.

Luminance–Voltage Characteristic

It is clear from the discussion above that the luminance-time pulses of Fig. 4 will become larger as the amplitude V_A of the applied voltage is increased. Integration of the luminance-time pulses in steady state over a fixed time period (say 1 s) is proportional to the device luminance in cd/m^2. A typical luminance–voltage characteristic is shown in Fig. 5. It is characterized by a threshold voltage (V_{TL}) below which little or no light is emitted (because the field is not sufficient for tunnel ejection of electrons from the interfaces). Above threshold, the luminance–voltage characteristics rise steeply (tunneling current increases exponentially with phosphor field or voltage) and finally saturate due to the exhaustion of activators that can be impact excited by the now numerous hot electrons, and other factors. This highly nonlinear luminance–voltage characteristic provides the device with the capability to be electrically addressed at a very high multiplexing ratio while maintaining excellent contrast. This is necessary for matrix addressing of high-information-content flat-panel displays. The typical performance level achievable in the 640 × 480 TFEL display units now on the market is a brightness of 45 fL and contrast ratios of 20 : 1 in a 500 lux ambient. Because these displays have wide viewing angles (>160°) and operate at video rates, EL technology has all the characteristics re-

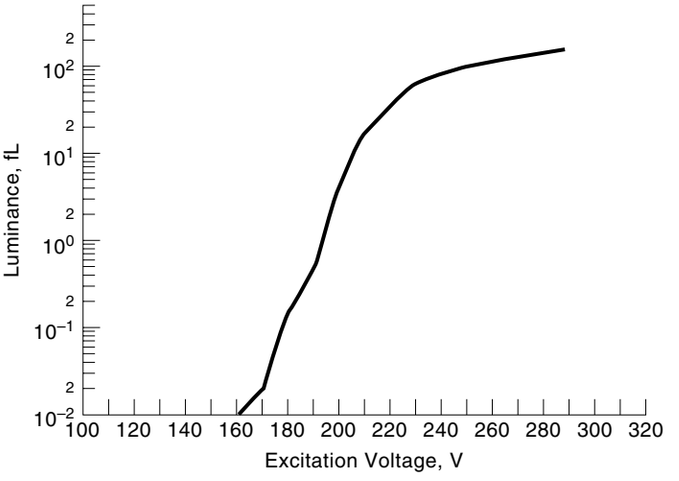

Figure 5. Luminance–voltage characteristic of an ACTFEL device. Note the threshold voltage (of 160 V) and the saturation effect typical of ACTFEL devices.

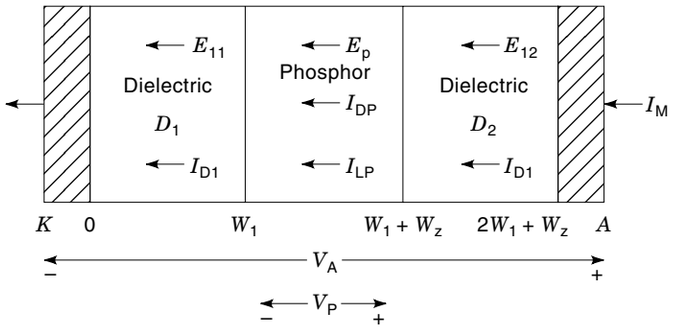

Figure 6. Schematic of an ACTFEL device structure showing various currents and fields.

quired to produce high-information-content flat-panel displays with the image quality of the CRT. The solid-state nature of EL displays makes them extremely rugged, which is often a desirable characteristic for a flat-panel display when used in portable applications (30).

Currents in Alternating Current Thin Film Electroluminance Devices

Consider an ACTFEL device of configuration shown in Fig. 6. The device is driven by bipolar voltage pulses shown in Fig. 7. Let $V_A(t)$ be the applied voltage; $V_P(t)$, the phosphor voltage; V_{PT}, the phosphor voltage at threshold; V_{AT}, the applied voltage at threshold; E_P, the electric field in the phosphor; E_{I1} and E_{I2} are electric fields in the insulators D_1 and D_2. $\in_P$ and $\in_I$ are dielectric constants of the phosphor and the dielectric layers and d_P and d_I are their thicknesses. A is the cross-section area of the device. C_P is the capacitance of the phosphor layer below threshold; C_I is the composite insulator capacitance; $C_T = C_P + C_I$; $C_d = C_P C_I/(C_P + C_I)$:

i_{D2} = displacement current in the insulator D_2

$$= A \in_I (dE_{12}/dt) \tag{11}$$

i_{DP} = displacement current in the phosphor layer

$$= A \in_P (dE_P/dt) \tag{12}$$

i_m = current measured by the probe in external circuit
i_{LP} = luminescence causing conduction current through the phosphor
$i_{LP} = 0$ below threshold ($V_A < V_{AT}$); $i_{LP} > 0$ above threshold [above threshold ($t_1 < t < t_4$), tunnel current is initiated in the phosphor]

$$i_m = i_{DP} + i_{LP} = i_{D2} \tag{13}$$

Thus, i_{LP} is obtained by subtracting the phosphor displacement current from the measured external current. The traditional technique for measurement of i_{LP} employs a capacitive bridge circuit and a differential amplifier (37). In essence the ACTFEL device is one arm of the bridge, while a balancing capacitor (C_B) constitutes the second arm. The value of C_B is adjusted to equal C_d, so that the output of the bridge circuit is zero below threshold. The device capacitance is then assumed to remain at C_d above threshold. Thus the current differential between the two arms of the bridge above threshold is assumed to equal i_{LP}. This technique amounts to setting $i_{DP} = C_d dV_A/dt$ in Eq. (13), so that,

$$i_{LP} = i_m - C_d(dV_A/dt) \tag{14}$$

The electric field in the phosphor is given by

$$E_P(t) = [C_I V_A(t) - \int_0^t i_{LP}(t)\, dt]/(C_T * d_p) \tag{15}$$

Combining Eqs. (12), (13), and (15), we obtain

$$i_{LP} = i_m(C_T/C_I) - C_P(dV_A/dt) \tag{16}$$

The above equations for phosphor field and current are valid only when there is no bulk space charge in the layer. Under certain conditions and especially when bulk space charge is present, these equations can yield inaccurate values for current and field. In that case, an iterative measurement technique described elsewhere (38) should be used. Figure 8 shows the equivalent circuit (37) of an ACTFEL which is useful for gaining a simplified insight into the workings of the device.

If one neglects the bulk space charge, the phosphor layer of an ACTFEL device can be represented by a fixed capacitor (C_P) below threshold. For simplicity, the phosphor layer above threshold is modeled as the same fixed capacitor (C_P) in parallel with a nonlinear element; the nonlinear element is used for describing the tunnel breakdown. The back-to-back diodes D_1 and D_2 represent idealized zener diodes. Several authors have used equivalent circuits like Fig. 8 or minor variations thereof. However, they do not explicitly include the effect of resistor R in their analysis of phosphor voltage. A more accu-

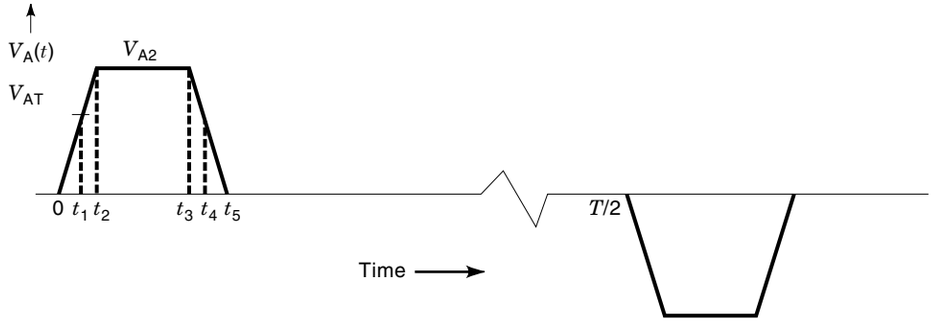

Figure 7. Waveform of the excitation voltage pulse. Typical values for the period T and pulsewidth are 10,000 μs and 30 μs, respectively.

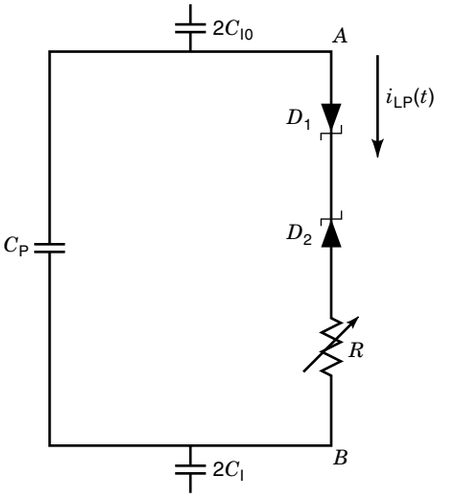

Figure 8. The equivalent circuit for the ACTFEL device. Diodes D_1 and D_2 model the breakdown of the phosphor layer.

rate equivalent circuit without this simplification has been described (39).

Transferred Charge, Power, and Luminance

Under the idealized conditions where the equivalent circuit of Fig. 8 is valid, one can compute the transferred charge (ΔQ) across the phosphor for each pulse, as follows.

Let $+Q_P$ and $-Q_P$ be the charges on the top and bottom capacitor plates of the phosphor layer capacitor, C_P, just below threshold when tunneling has not yet started, and the transferred charge across the phosphor is zero (see Fig. 8). The applied voltage is equal to the threshold voltage, V_T, which V_{PT} drops across the phosphor capacitance and $(V_T - V_{PT})/2$ across each insulator layer. For ease of conceptualization, we assume the two insulator layers to be identical. Note, however, that the final result would not be altered even if the two insulators were not identical. As the amplitude of the applied voltage is increased to V_A, the tunneling at the insulator–phosphor layer starts, the phosphor layer breaks down and the phosphor voltage is clamped at V_{PT}. As a result, all the excess applied voltage $(V_A - V_T)$ is dissipated across the two insulator layers, each taking an additional voltage of $(VA - V_T)/2$. Thus, *extra* charge (dQ) on the plates of each insulator capacitor (after threshold) is $2C_I(V_A - V_T)/2 = C_I(V_A - V_T)$. In other words, the top plate of each insulator capacitor has gained dQ, whereas the bottom plate has lost dQ. But the bottom plate of the upper insulator capacitor is the same as the top plate of the phosphor capacitor; also the top plate of the lower insulator is the bottom plate of the phosphor capacitor. Thus, one could say that the top plate of the phosphor capacitor has lost a charge of $dQ = C_I(V_A - V_T)$, whereas the bottom plate of the phosphor capacitor has gained a charge equal to $dQ = C_I(V_A - V_T)$. The charge transferred across the phosphor layer, ΔQ must therefore be given by

$$\Delta Q = dQ = C_I(V_A - V_T) \tag{17}$$

We note that this charge was transferred across the phosphor at a fixed (clamped) voltage of V_{PT}. Therefore, the work done on the phosphor during the pulse is,

$$W = C_I(V_A - V_T)V_{PT} \tag{18}$$

Because this work is done twice each cycle and there are f cycles per second, the power consumed by the device is

$$P = 2Wf = [2C_I(V_A - V_T)V_{PT}f] \tag{19}$$

Since one can think of V_T as the turn-on voltage and V_A as the operating voltage, $(V_A - V_T)$ is also called the modulation voltage, V_{mod}. It is interesting to note that after the tunnel current begins to flow, there is a charge ΔQ transferred across the phosphor layers but there is no change in voltage V_{PT}; it is as if the layer had an infinitely large ac capacitance dQ/dV.

For a typical commercial ACTFEL display (30), the values of the parameters in Eq. (19) are

$$C_I = 18\ \text{nF/cm}^2 \quad V_{mod} = 40\ \text{V} \quad V_{PT} = 90\ \text{V} \quad f = 60\ \text{Hz};$$
$$P = 7.7\ \text{mW/cm}^2 = 77\ \text{W/m}^2$$

This example illustrates that the power required to generate light from an ACTFEL display is quite small. For example, in a 10-in. diagonal, 640 × 480 pixel (VGA) ACTFEL display, with a pixel size of 0.022 cm × 0.022 cm, the total power dissipation would be

$$P_{DISS} = 7.7 \times 640 \times 480 \times (0.022) \times 0.022 = 1.15\ \text{W}$$

when all the pixels are on. If, on average, only half the pixels were on, then the display panel would consume only 0.57 W. This of course does not include the power consumption in the driver circuits, which could be as much as 10 W for the panel (40). To the first approximation, the light emission from an ACTFEL display device is directly proportional to the electrical power dissipated in the phosphor. Thus, the luminance, L is given by

$$L = \frac{\eta P_{DISS}}{\pi} = \frac{2\eta f C_I V_{MOD} V_{PT}}{\pi} \tag{20}$$

where η is the efficiency in lumens/watt. The factor, π in the denominator comes from the assumption of a perfectly diffusive surface of the EL device. In Eq. (20), the luminous efficiency is assumed to be independent of the electric field and phosphor thickness. Experimentally, luminous efficiency does increase with thickness at least over a limited range of thickness. Equation (20) also assumes that all charge is transferred at V_{PT}, when, in fact, charge will flow at higher voltages, depending on the voltage rise time. A typical value for η is 5 Lu/W, although much higher efficiencies have been achieved in some devices. Equation (20) gives the light emission in lumens. The conversion to calculate the brightness of the display, B in foot lamberts is,

$$B = (929\ \text{cm}^2/\text{ft}^2) * \text{L} \tag{21}$$

The above equations and the equivalent circuit are useful in analyzing the behavior of ACTFEL devices to a reasonable accuracy under the idealistic condition that no space charge is present in the bulk of the phosphor. In practice, this bulk charge plays a very important role in blue-emitting SrS:Ce

ACTFEL (41) as well as the yellow-emitting ZnS:Mn ACTFEL devices (42). Analytical and numerical methods for calculating current and luminance under those general conditions have been described (42).

Materials Issues

Requirements for the physical, electrical, and optical characteristics of materials used in the ACTFEL devices are described in this section.

Glass Substrate. Glass substrate should (1) be smooth, (2) be able to stand temperatures up to 650°C, (3) have low or no alkali-metal content,and (4) have high transmittivity in the visible-light region. Corning 7059 glass, Hoya NA-40, and soda lime glass with a barrier layer have been used (43).

Transparent Conducting Electrode. This layer should have, (1) low resistivity—a resistivity of less than $10^{-4}\ \Omega \cdot$ cm is desirable, (2) small thickness—a thickness of less than 150 nm is desirable, (3) low sheet resistance—a typical value is 5 to 10 Ω/square; and (4) high transmittivity in the visible light region.

Typically, an ITO film is used for this layer, although $CdSnO_3$ and ZnO have been used in laboratory samples.

Insulating Layers. The purpose of the insulating layers is to protect the phosphor layer from electrical breakdown; therefore, they should be defect-free. Other requirements include (1) high breakdown field, a value in excess of 3 MV/cm is needed; (2) high dielectric constant; (3) small tan δ loss, and (4) a small number of pinholes.

A large number of dielectric materials including Al_2O_3, SiO_2, SiON, Y_2O_3, and $BaTiO_3$ have been used. A useful figure of merit for this layer is the product of the dielectric constant and the breakdown field. $Sr(Zr,Ti)O_3$ films deposited by sputtering have a relative dielectric constant of 100, a breakdown field of 3 MV/cm and a figure of merit value of 26 μC/cm^2 (44).

Phosphor Layers. Phosphor layers in ACTFEL displays contain the host material and luminescent (activator) centers. The host material (1) must be able to withstand a high electric field (1 MV/cm) before breakdown, (2) should be an insulator at fields below breakdown, (3) should have a bandgap larger than the energy of the photons being emitted by the luminescent centers imbedded in it (otherwise the emitted light will be absorbed by the host material before it can leave the ACTFEL device; typically, a bandgap in excess of 3 eV is required), and (4) should be able to transport significant current densities of hot electrons. It has been found empirically that host phosphor materials with bandgaps in excess of 4.5 eV cannot carry significant conduction current and are not suitable as EL phosphors. In practice, host materials satisfying the above conditions have been II–VI compounds, like ZnS, SrS, CaS, ZnSe, and SrSe and alkaline earth thiogallates, like $SrGa_2S_4$, $CaGa_2S_4$, and $BaGa_2S_4$.

The requirements on the luminescent (or activator) centers are (1) large cross section for impact excitation, (2) stability in the high field environment of an ACTFEL device (~1 MV/cm), (3) emission in the visible-light spectrum, (4) compatibility with the host phosphor material in terms of ion size, charge, and so on.

Table 2. Electroluminescent Phosphor Performance Summary

Phosphor Material	Emission Color	CIE x	CIE y	L(cd/m^2) @ 60 Hz	Efficiency lm/W
ZnS : Mn	Yellow	0.50	0.50	300	3–6
CaS : Eu	Red	0.68	0.31	12	0.2
ZnS : Mn/filter	Red	0.65	0.35	65	0.8
ZnS : Tb	Green	0.30	0.60	100	0.6–1.3
SrS : Ce	Bluegreen	0.30	0.50	100	0.8–1.6
$SrGa_2S_4$: Ce	Blue	0.15	0.10	5	.02
$CaGa_2S_4$: Ce	Blue	0.15	0.19	10	.03
ZnS : Mn/SrS : Ce	"White"	0.44	0.48	470	1.5

Among the luminescent centers used in ACTFEL devices are manganese, terbium, samarium, thulium, europium, and cerium.

Opaque Electrodes. The requirements for the back electrode are (1) low resistivity, (2) adhesion to the insulating layer, (3) no metal-ion migration at high field, and (4) an ability to prevent the spread of dielectric breakdown in the device. To date, aluminum has been the most preferred electrode material for this purpose.

Phosphor Materials for Color Alternating Current Thin Film Electroluminescent Displays

A major challenge faced by the EL industry today is the development of efficient EL phosphor materials for the primary (red, green, and blue) colors, so that a full color display may be realized (30). An efficient red (1 lm/W) has now been achieved with the combination of the standard ZnS:Mn yellow phosphor and a red filter (45). The green ZnS : Tb phosphor also has an efficiency near 1 lm/W (46). The best blue phosphor available until just recently was SrS : Ce which, although efficient (>1.0 lm/W) actually has a blue-green chromaticity (x = 0.19, y = 0.38). Thus blue still remains a challenge. Table 2 summarizes the performance of various electroluminescent phosphors. Another approach toward a full-color display has been the development of an efficient white (or broadband) phosphor that can be filtered to produce red, green, and blue colors. This is called the *color by-white* approach. Recent results in the development of white and blue phosphors can be found elsewhere (30).

Also, several device designs for color ACTFEL displays have been developed. These include (1) the multicolor display, (2) the broadband white phosphor with a patterned color filter, and (3) the dual substrate full color panel. An excellent discussion of these designs and their performance can be found elsewhere (30).

Active Matrix Electroluminescent Devices for Head-Mounted Displays

Electroluminescent devices are well suited for the small, high-resolution displays needed for head-mounted-display (HMD) applications. For HMD, the diagonal display size is in the 0.5–2 in. range. Thus a resolution of 1000 lines/in. would be needed for a 640 × 480 video graphic array (VGA) display with a diagonal of 0.7 in. or a 1280 × 1024 display with a diagonal of 1.7 in. (30).

Since passive display panels with drivers connected around the perimeter are limited to approximately 500 lines per inch (lpi) resolution, an active matrix approach becomes necessary for HMD applications. Active matrix electroluminescent (AMEL) displays of 24 μm pixel size and a resolution of more than 1000 lpi have been demonstrated. Typical performance characteristics for the AMEL VGA display include brightness of 50 fL and contrast ratio greater than 100 : 1 with a typical power consumption of 200 mW. This display is 0.76 in. diagonally, has a thickness less than 2 mm, and weighs less than 4 g, so it is quite easy to integrate the display and optics into very light head gear for HMDs that are no more obtrusive than a pair of eye glasses. The electrical and optical performance of this high-resolution display combined with its small size and weight provides a powerful new display technology for portable systems.

BIBLIOGRAPHY

1. M. J. Hoskins and B. J. Hunsinger, Simple theory of buried channel acoustic charge transport in GaAs. *J. Appl. Phys.,* **55** (2): 413–426, 1984.
2. M. J. Hoskins and B. J. Hunsinger, Recent developments in acoustic charge transport devices, *IEEE Ultrason. Symp. Proc.,* 1986.
3. B. M. Hunsinger, SAWs enable the advent of the signal microprocessor development station, *Proc. IEEE Ultrason. Symp.,* 225–229, 1990.
4. J. E. Bales, M. J. Hoskins, and P. H. Sahm, A GaAs ACT/IC programmable wide-band analog signal processor, *Proc. 1990 IEEE GaAsIC Symp.,* 23–26, 1990.
5. R. W. Miller and R. J. Kansy, Acoustic charge transport digitally programmable transversal filter development. *1990 IEEE MTT-S Symp. Proc.,* 1111–1114, 1990.
6. H. R. Stocker et al., Octave bandwidth high performance SAW delay lines, *1990 IEEE MTT-S Symp.,* 386–390, 1990.
7. M. Kowatsch et al., Analog encoded chirp transmission system using surface acoustic wave filters, *IEEE Trans. Sonic Ultrason.,* **SU-27**, 1980.
8. H. R. Stocker et al., Surface wave pulse compression filters with long chirp time, *Proc. IEEE Ultrason. Symp.,* 78–82, 1981.
9. C. W. Ruppel, SAW devices for consumer communication applications, *IEEE Trans. Ultrason., Ferroelectr. Freq. Control,* **40**: 438–452, 1993.
10. K. Y. Wong, Surface acoustic waves for high resolution radar, M.S. Thesis, The University of Texas at El Paso, July 1993.
11. O. Campbell, *Surface Acoustic Wave Devices and Their Signal Processing Applications,* San Diego: Academic Press, 1989.
12. A. J. Vigil et al., Application of Acoustic Charge Transport, *IEEE Trans. Ultrason. Ferroelectr. Freq. Control,* **40**: 488–495, 1993.
13. I. Deyhimy et al., *Appl. Phys. Lett.* **32**: 383, 1978.
14. A. van der Ziel, *Solid State Electron.* **20**: 269, 1977.
15. C. Kocot and C. A. Stolte, *IEEE Trans. Electron Devices,* **ED-29**: 1059, 1982.
16. S. Datta and B. J. Hunsinger, *J. Appl. Phys.,* **49**: 475, 1978.
17. N. I. Meyer and M. H. Jorgensen, in *Festkorperprobleme X,* 1st ed., New York: Pergamon, 1970, pp. 21–231.
18. H. F. Tierstein, Thickness vibrations of piezoelectric plates, *J. Acous. Soc. Amer.,* **35**: 53–58, 1963.
19. M. G. Holland and L. T. Claiborne, Practical surface acoustic wave devices, *Proc. IEEE,* **62**: 582–611, 1974.
20. D. C. Scheleher, *Electronic Warfare.* Dedham, MA: Artech House, 1986.
21. D. Bursky, DSPs expand role as cost drops and speed increases, *Electron. Des.,* 53–81, 1991.
22. W. R. Smith, SAW filters for CPSM spread spectrum communications, *IEEE Ultrason. Symp. Proc.,* 524–528, 1977.
23. B. Widrow and S. D. Stearns, *Adaptive Signal Processing.* Englewood Cliffs, NJ: Prentice-Hall, 1985.
24. M. J. Miller and M. J. Hoskins, *Acoustic Charge Transport Real-time Image Processor,* Final Tech. Rep., USAF/WL Contract N. F08635-90-C-0498.
25. M. J. Russ and D. I. Kennedy, *J. Electrochem. Soc.,* **114**, 1066, 1967.
26. T. Inoguchi et al., *Dig. 1974 SID Int. Symp.,* 84, 1974.
27. S. Mito et al., *Dig. 1974 SID Int. Symp.,* 86, 1974.
28. Y. A. Ono, *Electroluminescent Displays,* New York: World Scientific, 1995, p. 4.
29. W. Barrow et al., *Conf. Record 1994 Int. Display Res. Conf.,* 448, 1994.
30. C. N. King, SID-96 Seminar Lecture Notes, **I**, *Soc. Inf. Display,* Santa Ana, CA, 1996, p. M-9/5.
31. Ref. 28, Ch. 6.
32. Ref. 28, Ch. 5.
33. V. P. Singh et al., Modification and characterization of insulator-semiconductor interface in A.C. Thin film electroluminescence display devices, *Proc. Int. Electron Devices Meet.,* San Francisco, December 13–16, 1992, pp. 27.6.1–27.6.4.
34. A. Aguilera, V. P. Singh, and D. C. Morton, Electron Energy Distribution at the Insulator-Semiconductor Interface in A.C. Thin Film Electroluminescent Display Devices, *IEEE Trans. Electron Devices,* **41**: 1357–1363, 1994.
35. V. P. Singh et al., PECVC silicon nitride—aluminum oxide dielectric layer stacks for reduced current crowding in ZnS : Mn ACTFEL display devices, *Proc. IDRC / Euro Display,* **16**: 211–214, 1996.
36. V. P. Singh, S. Bhaskaran, and J. C. McClure, Current crowding and phosphor efficacy in ACTFEL display devices, *J. Soc. Inf. Display,* **4** (2): 59–63, 1996.
37. P. M. Alt, Thin-film electroluminescent displays: device characteristics and performance, *Proc. SID,* **25** (2): 123–145, 1984.
38. V. P. Singh, S. Knishna, and D. C. Morton, Electric field and conduction current in ac thin-film electroluminescent display devices, *J. Appl. Phys.* **70** (3): 1811–1819, 1991.
39. V. P. Singh et al., Phosphor currents in ZnS : Mn ac thin film electroluminescent display devices, *J. Appl. Phys.,* **72** (9): 4148–4155, 1992.
40. Ref. 28, Ch. 8.
41. V. P. Singh and D. C. Morton, A model for electroluminescence in SrS : Ce ACTFEL display devices, *IEEE Trans. Electron Devices,* **39**: 1331–1340, 1992.
42. V. Singh, W. Majid, and D. Morton, Analysis of ZnS : Mn type a.c. thin film electroluminescent display devices with bulk traps, *J. Soc. Inf. Display,* **1** (2): 135–141, 1993.
43. T. Suntola and J. Hyrärinen, *Ann. Rev. Mater. Sci.,* **15**, 177, 1985.
44. Ref. 28, p. 65
45. R. T. Tuenge and J. Kane, Bright red EL using a thin-film filter, *Dig. 1991 SID Int. Symp.,* 279, 1991.
46. G. Härkönen, K. Härkönen, and R. Törnqvist, Green emetting thin film electroluminescent device grown by atomic layer epitaxy, *Dig. 1990 SID Int. Symp.,* 232, 1991.

VIJAY P. SINGH
The University of Texas at El Paso

ACOUSTIC ECHO CANCELLATION. See ECHO CANCELLATION FOR SPEECH SIGNALS.

ACOUSTIC FLOW MEASUREMENT, MEDICAL. See FLOW TECHNIQUES, MEDICAL.

ACOUSTIC MICROMECHANICAL DEVICES. See MICROMECHANICAL ACOUSTIC AND ULTRASONIC DEVICES.